Materials Research Bulletin 44 (2009) 2092–2098

Contents lists available at ScienceDirect

Materials Research Bulletin

journal homepage: www.elsevier.com/locate/matresbu

Substitutional nitrogen-doped tin oxide single crystalline submicrorod arrays: Vertical growth, band gap tuning and visible light-driven photocatalysis

S.S. Pan [a,b], Y.D. Shen [b], X.M. Teng [a], Y.X. Zhang [a], L. Li [a], Z.Q. Chu [a], J.P. Zhang [a], G.H. Li [a,*], X. Hu [b,*]

[a] Key Laboratory of Materials Physics, Anhui Key Laboratory of Nanomaterials and Nanostructures, Institute of Solid State Physics, Chinese Academy of Sciences, Hefei 230031, PR China
[b] School of Materials Science & Engineering, Nanyang Technological University, Nanyang Avenue, 639798, Republic of Singapore

ARTICLE INFO

Article history:
Received 23 February 2009
Received in revised form 9 June 2009
Accepted 14 July 2009
Available online 24 July 2009

ABSTRACT

High-density substitutional N-doped SnO_2 submicrorod arrays were grown on Si and quartz substrates by catalysts-free reactive sputtering. Scanning electron microscope and high-resolution transmission electron microscopy results show that the submicrorods are vertically aligned single crystal with quasi-tetrahedral pyramid shape nanotip at the top end. The density and the shape of the submicrorods can be modulated by the nitrogen partial pressure. Ellipsometry and optical absorption characterization show that after substitutional N-doping, the band gap of N-doped SnO_2 submicrorod shifts toward visible light region (up to 624 nm), and the visible light absorption are significantly enhanced due to the band gap narrowing. The photodegradation of methylene blue by N-doped SnO_2 submicrorod under visible light illumination is demonstrated, and it was found that the surface-to-volume ratio plays an important role in achieving high photocatalytic reactivity. The SnO_2:N submicrorod arrays with visible light band gap may have potential applications in solar cells electrode and visible light sensitive photocatalyst.

1. Introduction

Recently, there has been great interest in searching and developing semiconductor photocatalysts with high visible light activities, which can harness the sunlight energy high efficiently, for environmental and energy source applications, such as indoor air purification, water decontamination and hydrogen generation from water [1]. Among them, semiconductor oxides with non-toxicity, low cost, high stability have attracted more and more attention. SnO_2 is a multifunctional wide band gap semiconductor oxide, and has wide applications due to its outstanding optical and electrical properties accompanied with superior mechanical and chemical stability [2].

It is well known that SnO_2 is a visible light inactive photocatalyst due to its wide band gap of 3.6 eV in ultraviolet band, and the electron cannot be excited from valence band to conduction band by visible light activation [3]. In general, the following strategies can be adopted to promote visible light-driven photocatalytic activity of semiconductors: doping, microstructure morphological and crystal phase modulation, surface modification, hetero-composite materials. In most cases, SnO_2 has been mixed with other photocatalysts and forms binary heterostructures, such as TiO_2, ZnO, etc., or microstructure modification to activate its photocatalysis activity [3–6]. However, there are few reports about the intrinsic visible light sensitive photocatalysis of SnO_2 caused by doping-induced band gap narrowing.

The substitutional nitrogen doping in oxides is a most effective method to red-tune their band gap because its p states contribute to the band gap narrowing by mixing with O 2p states. N-doped SnO_2 (hereafter referred as SnO_2:N) films can be prepared by magnetron reactive sputtering in gas mixtures of nitrogen and oxygen as described elsewhere [7]. It was found that the band gap of SnO_2:N film decreases with increasing nitrogen partial pressure in sputtering deposition [7]. However, earlier work on N-doped SnO_2 showed only limited band gap shift because of substitutional nitrogen doping have not been achieved [7–9]. Conventional film deposition methods, such as sputtering and pulsed laser deposition (PLD), are greatly attractive for nanostructures growth; because they are highly repeatable and controllable, facilely adapted to tune the physical properties of materials by alloying or doping, and entirely compatible with the current thin film technology and device fabrication. In comparison to powder photocatalysts, the nanostructure photocatalysts with high surface-to-volume (S/V) ratio grown on certain substrates are more feasible to be collected, recycled and pre-/post-treated. In this paper, we report the preparation of SnO_2:N submicrorod arrays by reactive sputtering under high nitrogen gas partial ratio (>95%). The band gap tuning by atomic N (substitutional N) doping and the visible light-driven

* Corresponding authors. Tel.: +86 551 5591437; fax: +86 551 5591434.
E-mail addresses: ghli@issp.ac.cn (G.H. Li), asxhu@ntu.edu.sg (X. Hu).

0025-5408/$ – see front matter © 2009 Elsevier Ltd. All rights reserved.
doi:10.1016/j.materresbull.2009.07.011

photocatalytic behavior are demonstrated. The growth mechanisms of the doped submicrorods are also discussed.

2. Experimental details

Wafers of polished n-type Si (1 0 0) and quartz were used as substrates and ultrasonically cleansed in acetone and ethanol before introducing into the deposition chamber. The SnO_2:N submicrorods were grown on Si and quartz substrates by radio frequency magnetron reactive sputtering technique with power of 100 W. The base pressure of the deposition chamber is about 5.0×10^{-5} Pa. The metal Sn target (purity: 99.99%) and the gas mixtures of high purity nitrogen (purity: 99.999%) and oxygen (purity: 99.999%) were used as sputtering material and working gas, respectively. The N_2 flux ratio was defined as $F_{N_2} = f(N_2)/[f(N_2)+f(O_2)]$, where $f(N_2)$ and $f(O_2)$ are the individual flux of the N_2 and O_2 gas, respectively. In this study, the SnO_2:N submicrorods were deposited under high nitrogen partial pressure, and nitrogen F_{N_2} was set as 98.4, 97 and 95%. The substrate temperature and the total gas pressure were kept at 400 °C and 3.2 Pa, respectively. The substrate was rotated at 10 rpm for the improvement of the sample homogeneity. The details of the deposition parameters are listed in Table 1.

The crystalline structure was examined by X-ray diffractometer (XRD, θ–2θ, Philips X'Pert Pro MPD, Cu K_α). A FEI Sirion 200 field emission type scanning electron microscope (FESEM) was used to observe the morphologies of the SnO_2:N submicrorods. High-resolution transmission electron microscopy (HRTEM, JEOL-2010) with selected-area electron diffraction (SAED) analyses was used to study crystalline structures and morphologies of submicrorods. Absorption spectra were measured with a double beam spectrometer at UV–vis spectrometer (Varian Cary 5E). An ex situ phase modulated spectroscopy ellipsometry (SE, model UVISEL Jobin-Yvon) in the spectral range of 1–6 eV with a step of 0.05 eV at an incidence angle of 70° was used to determine the thickness and optical properties of the films. X-ray photoelectron spectroscopy (XPS, Kratos Axis-Ultra, monochromated Al-K alpha) was used to determine the chemical bonding states of the films.

For the photocatalysis experiment, the methylene blue (MB) was used as test organic molecules. The specimen was immersed in the 2.5 mL MB aqueous solution with concentration of 5.0×10^{-5} M and irradiated from a 300 W Xe arc lamp with UV cutoff filter (providing visible light with $\lambda > 380$ nm). The distance between Xe lamp and sample was 1.5 m, and the heat effect from light source can be eliminated efficiently. At given time intervals, the photodegraded solution was analyzed with a UV–vis spectrophotometer (Shimadzu, UV-2501 PC) by recording variations of the absorption band maximum (~664 nm) in the UV–vis spectrum of MB.

3. Results and discussion

3.1. Structure characterization

Fig. 1 shows XRD patterns of the SnO_2:N submicrorods on quartz and Si substrates grown with different nitrogen partial pressures F_{N_2}. The observed SnO_2:N submicrorods diffraction peaks correspond to a typical SnO_2 cassiterite phase (JCPDS File No. 88-0287) [10]. No diffraction peaks coming from tin, tin nitride or other tin oxide could be observed, suggesting that nitrogen atoms might substitute oxygen sites in SnO_2 lattice.

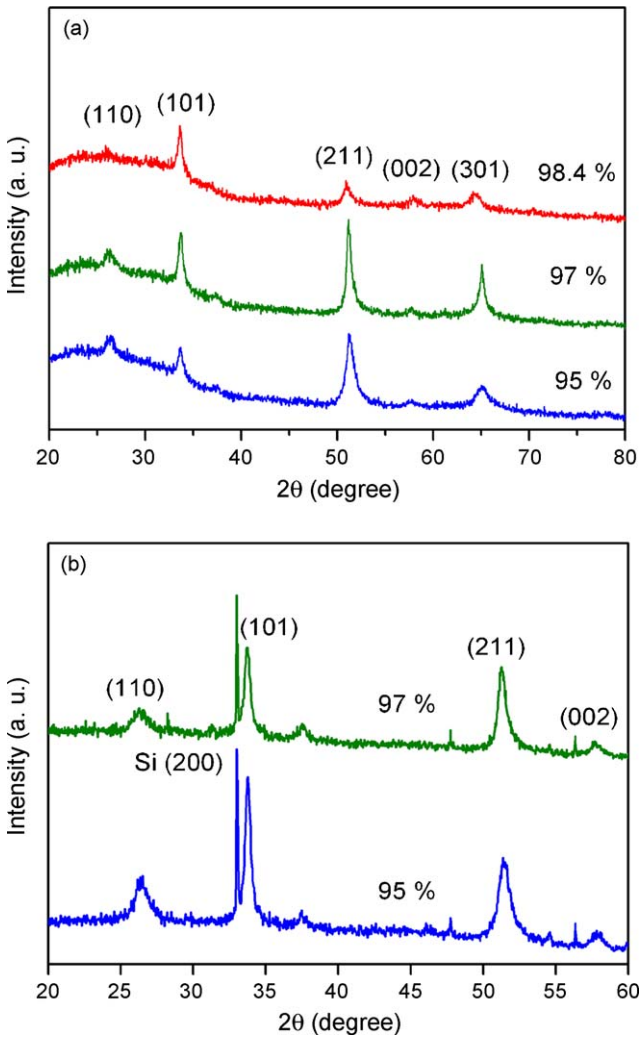

Fig. 1. XRD patterns of SnO_2:N submicrorod arrays with different F_{N_2} on (a) quartz and (b) Si substrates.

The degree of preferential orientation for the films was determined, following subtraction of background radiation, by calculation of a texture coefficient, τ, defined as [11].

$$\tau = \frac{I_m(h\,k\,l)/I_0(h\,k\,l)}{(1/n)\sum_1^n I_m(h\,k\,l)/I_0(h\,k\,l)} \quad (1)$$

where $I_m(h\,k\,l)$ is the measured relative intensity of the reflection from the $(h\,k\,l)$ plane, $I_0(h\,k\,l)$ is the relative intensity from the same plane in a standard reference sample (JCPDS: 88-0287), and n is the total number of reflection peaks considered in analysis. The texture coefficients of the SnO_2:N submicrorods with different F_{N_2} calculated form the XRD data are shown in Table 2. From Table 2

Table 1
Deposition parameters of SnO_2:N submicrorods by reactive sputtering.

N_2 gas ratio	Gas flux (sccm)	Deposition time (min)	Deposition rate (nm/min)	Self-bias voltage (V)
98.4%	N_2-49.2; O_2-0.8	80	13.8	327
97%	N_2-48.5; O_2-1.5	85	12.5	322
95%	N_2-47.5; O_2-2.5	90	10.8	325

Table 2
Texture coefficient and standard deviation of the SnO_2:N submicrorods on quartz with (F_{N_2} = 97 and 95%).

Sample	N_2 gas ratio	$\tau_{(1\,1\,0)}$	$\tau_{(1\,0\,1)}$	$\tau_{(2\,1\,1)}$	$\tau_{(3\,0\,1)}$
S2	97%	0.16401	0.40836	0.76743	2.66019
S3	95%	0.24448	0.42815	1.47318	1.8542

Table 3
Lattice parameters of SnO_2:N submicrorods.

N_2 gas ratio	Lattice spacing (Å)	lattice parameters (Å)
97%	$d_{(1\,1\,0)}$: 3.3828	a = 4.8021
	$d_{(1\,0\,1)}$: 2.6579	c = 3.1914
	$d_{(2\,1\,1)}$: 1.7817	
95%	$d_{(1\,1\,0)}$: 3.3772	a = 4.7839
	$d_{(1\,0\,1)}$: 2.6551	c = 3.1917
	$d_{(2\,1\,1)}$: 1.7771	

one can see that the SnO_2:N submicrorod arrays show highly [2 1 1] and [3 0 1]-oriented growth.

The relationship between the ($h\,k\,l$) interplanar spacing of tetragonal phase and the lattice parameters of a and c is shown as follows:

$$d_{hkl} = \frac{a}{\sqrt{h^2 + k^2 + l^2(a^2/c^2)}} \quad (2)$$

To determine the lattice parameters accurately, high-resolution XRD analysis of SnO_2:N on Si wafer was performed, and the result is shown in Fig. 1(b). The (2 0 0) diffraction peak from Si wafer was adopted as calibration to monitor the position shift of the specimen stage, and the lattice parameters of SnO_2:N submicrorods calculated from Eq. (2) are listed in Table 3. One can see that the crystal lattice of SnO_2:N expands after nitrogen doping, and the crystal lattice expansion is along a-axis predominantly, which might be due to the substitution of N for O ion.

The dissociation energy of nitrogen and oxygen molecule is 9.756 and 5.11 eV [12], respectively, and the chemical activity of oxygen is much higher than nitrogen. Though the partial pressure of nitrogen is extremely high (>95%) as compared with that of oxygen in the reactive sputtering, the Sn prefers reacting with the oxygen with higher chemical activity, and the nitrogen acts as a dopant.

The elements in resultants are only tin, nitrogen and oxygen determined from the X-ray photoelectron spectroscopy (XPS) survey. To investigate N states in $SnO_{2-x}N_x$, we measured N 1s core levels with high-resolution XPS, as shown in Fig. 2. Three peak structures with the binding energies of about 396, 399, and 402 eV were observed in N-doped SnO_2 submicrorod arrays. According to previous XPS works on tin nitride and other N-doped oxides [15], we attribute the N 1s peak with binding energy of 396 eV to the atomic nitrogen, "β-N", namely, the O in crystal lattice substituted by N in $SnO_{2-x}N_x$. It should be pointed out that atomic nitrogen

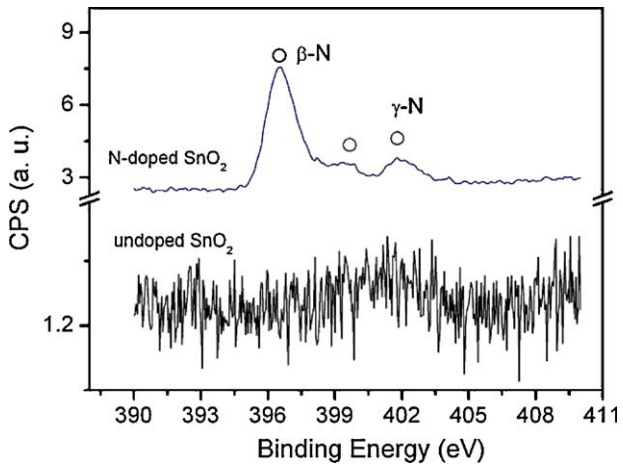

Fig. 2. N 1s XPS spectra of the (upper lines) SnO_2:N submicrorod arrays and the undoped SnO_2 films (lower lines).

doping is considered to be indispensable for band gap narrowing and inducing the visible light-driven photocatalysis activity of TiO_2 and other oxide photocatalysts [1].

Fig. 3 shows the cross-section and top view FESEM images of SnO_2:N submicrorods with different N_2 flux ratio F_{N_2}. Three well-defined regions can be clearly seen: (1) a rather compact film layer near the substrate, (2) an upper layer where the submicrorods are vertically isolated from each other, and (3) a rough surface layer consisting of SnO_2:N nanotips and void. These results indicate that the submicrorod arrays are grown on a buffer layer formed at the initial stage of the deposition. The stem has a coarse and corrugated side surface, showing a stacked-lamella structure, while the cone tip shows a smooth surface. The lateral sizes of the cones are between 50 and 150 nm while the apical tip radius are only about several nanometers. The heights of the submicrorods are almost uniform and can be controlled simply by the growth time. The submicrorod arrays with different F_{N_2} have different shapes: ellipsoid-like tips (98.4%) and pyramid-like tetrahedron (95 and 97%). For the SnO_2:N with F_{N_2} = 95 and 97%, the top end of the submicrorod has a quasi-tetrahedral pyramid-like shape with many layers, indicating that the submicrorods grow along a preferential direction and follow the epitaxial layer-by-layer growth mode. In this study, the SnO_2:N submicrorod arrays were grown at low substrate temperature (~400 °C) without using any catalysts and templates, and in situ atomic nitrogen doping has been facilely realized.

The atomic structure of an individual SnO_2:N submicrorod with F_{N_2} = 95% were further investigated by HRTEM analyses, and the results are shown in Fig. 4. The clear lattice fringes in Fig. 4(a) and (b) demonstrate an interplanar spacing of 3.36 and 2.64 Å, corresponding to the (1 1 0) and (1 0 1) plane of tetragonal SnO_2:N with a rutile structure, respectively, which are well consistent with XRD results listed in Table 3. The sharp diffraction spots in the selected-area electron diffraction pattern shown in Fig. 4(c) further proved that the SnO_2:N submicrorods are single crystalline.

For the tetragonal crystal structures with lattice parameters of a and c, the inclination between the ($h_1\,k_1\,l_1$) and ($h_2\,k_2\,l_2$) plane can be determined from the following equation:

$$\cos\Phi = \frac{(h_1h_2 + k_1k_2/a^2) + (l_1l_2/c^2)}{\sqrt{((h_1^2 + k_1^2/a^2) + (l_1^2/c^2))((h_2^2 + k_2^2/a^2) + (l_2^2/c^2))}} \quad (3)$$

For SnO_2:N (F_{N_2} = 95%) submicrorods, the a and c are 4.78 and 3.19 Å (see Table 3), respectively, and the inclination between the (1 1 0) and (1 0 1) planes calculated from Eq. (3) is about 66.89°. The inclination between the (1 1 0) and (1 0 1) planes can be directly measured from the HRTEM lattice image, and the corresponding stripes show an orientation difference of 67°, which is in well accordance with the calculated value.

3.2. Growth mechanisms of SnO_2:N single crystalline submicrorod arrays

In this study, the SnO_2:N submicrorods are obtained under a typical vertical growth condition without using any external catalysts used, and is considered dominated by a vapor–solid (V–S) mechanism [13,14].

It is well known that the film growth proceeds through consecutive structure evolution stages: nucleation, island growth, coalescence of islands, development of continuous structure, and thickness growth [13]. The initial nucleation of SnO_2:N on the silicon or quartz substrate follows a three-dimensional island growth mechanism, and islands with a random crystallographic orientation are distributed on the substrate. At coalescence, the island with the highest perpendicular growth speed will overgrow the others, the subsequent growth proceeds by adhesion to

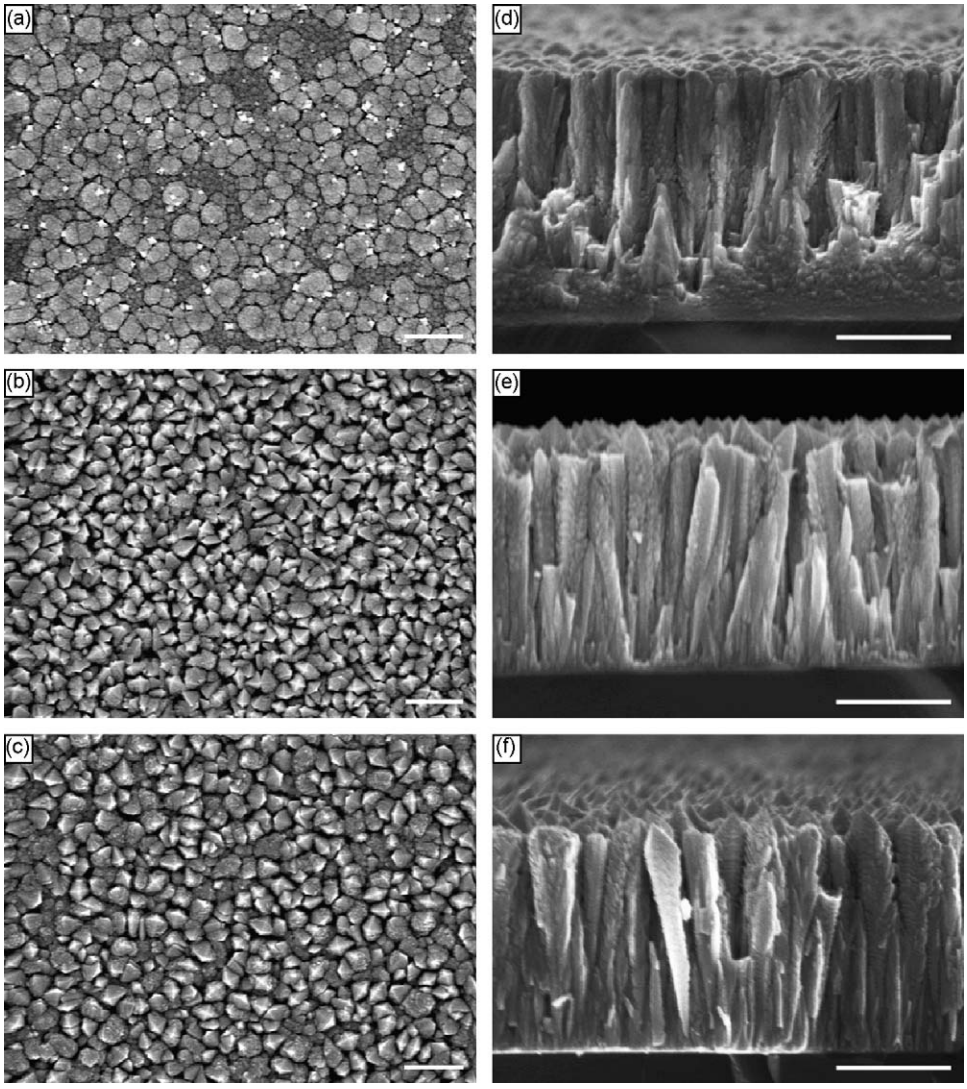

Fig. 3. Top view and cross-sectional FESEM images of SnO_2:N submicrorod arrays on Si substrate with N_2 flux ratio F_{N_2} of 98.4% (a and d), 97% (b and e), 95% (c and f); scale bar: 500 nm.

existing sites, yielding 1D vapor–solid growth of distinct SnO_2:N submicrorods. Once nucleated, subsequent perpendicular growth of these SnO_2:N submicrorods is apparent. The growth rate of the SnO_2:N submicrorods deposited at high nitrogen partial pressure is very high as comparison with the SnO_2:N thin films deposited at low nitrogen partial pressure reported in a previous study [9]. The increased growth rate of the SnO_2:N submicrorods with nitrogen partial pressure also can be seen in Table 1. The high deposition rate is considered to promote the perpendicular growth of SnO_2:N submicrorod. The quasi-tetrahedral pyramid-like nanotip can be attributed to the rutile-type crystal structure of SnO_2:N, which is a tetragonal phase with the space group $P4_2/mnm$ [10].

It appears that nucleation and growth of well-aligned submicrorods with uniform distribution does not occur until a layer of SnO_2:N with sufficient thickness is accumulated on the substrate (see Fig. 3), providing more energetically favorable planes for 1D growth in different directions. The single crystalline submicrorod arrays are epitaxially grown on pre-deposited SnO_2:N seed layer. Initially, grains of the condensed layer are randomly oriented. As condensation continues, an Ostwald ripening-like process takes place: grains with energetically favorable crystallographic planes will preferentially grow, while those with energetically unfavorable surfaces gradually shrink and eventually disappear [14].

3.3. Optical properties

Fig. 5 shows the optical absorption spectra of the SnO_2:N submicrorod arrays on quartz substrates with different nitrogen partial pressures. The absorption edge shifts toward longer wavelength side, and the absorption in the visible region increases with increasing nitrogen ratio in the SnO_2:N submicrorod arrays. The redshift of the absorption edge can be attributed to the decreases of SnO_2:N band gap with increasing nitrogen concentration [7]. As SnO_2:N submicrorods could be used as semiconductor electrode for harvesting solar energy, the redshift of the absorption edge and the enhanced visible light absorption will greatly increase the solar energy conversion efficiency in solar cell. From the absorption curve of SnO_2:N, the initial photon energies of strong absorption region (i.e. absorption coefficient $\alpha > 10^4\ cm^{-1}$) are about 688, 451, and 444 nm (corresponding photon energy: 1.8, 2.75, and 2.8 eV) for $F_{N_2} = 98.4,\ 97$ and 95%, respectively.

To determine the optical constants of the SnO_2:N submicrorod arrays, a four-layer model on quartz substrate was built based on the microstructure characterization: the interface layer (L_1), initial homogeneous SnO_2:N layer (L_2), porous SnO_2:N submicrorods layer consists of void and SnO_2:N submicrorods (L_3), and surface rough layer consists of void and SnO_2:N nanotips (L_4). The Tauc-Lorentz (TL) dispersion model was adopted to describe the

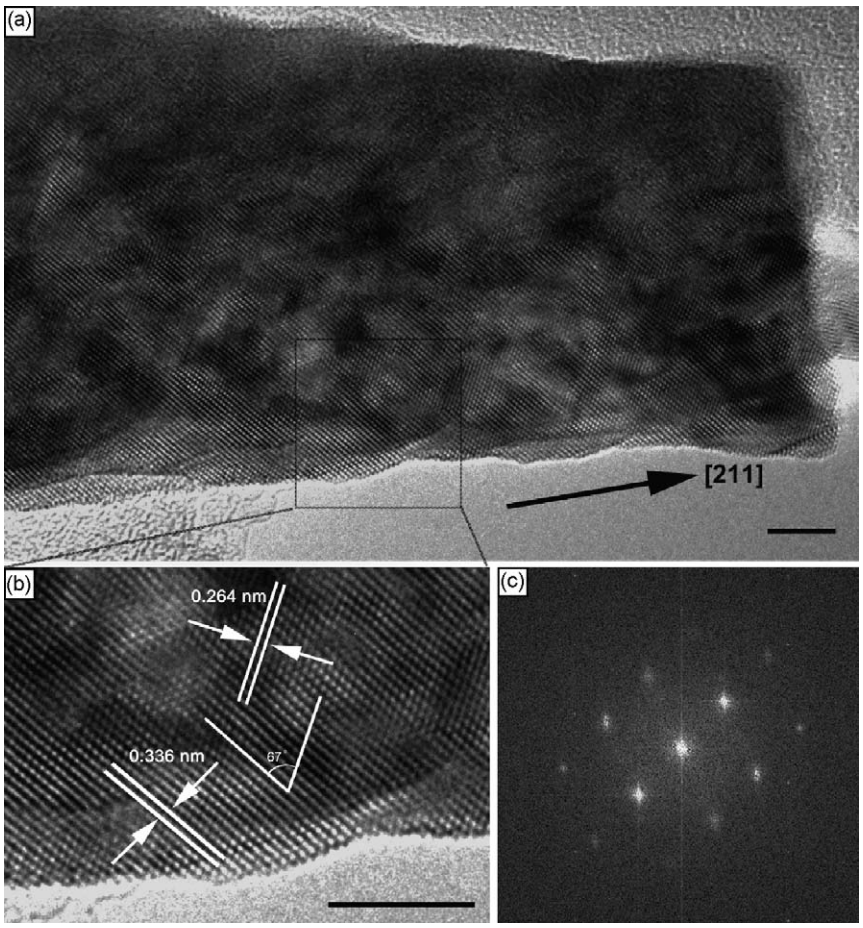

Fig. 4. (a) HRTEM image of a single SnO_2:N submicrorod ($F_{N_2} = 95\%$), (b) the corresponding local pattern and (c) SAED pattern; scale bar: 5 nm.

dielectric function of the SnO_2:N submicrorod array as expressed in the following [7]:

$$\varepsilon_i(E) = \begin{cases} \dfrac{AE_0C(E-E_g)^2}{\left(E_2-{E_0}^2\right)^2 + C^2E^2}\dfrac{1}{E} & (E > E_g) \\ 0 & (E \le E_g) \end{cases} \quad (4)$$

$$\varepsilon_r(E) = \varepsilon_\infty + \frac{2P}{\pi}\int_{E_g}^{\infty}\frac{\xi\varepsilon_2(\xi)}{\xi^2 - E^2}d\xi \quad (5)$$

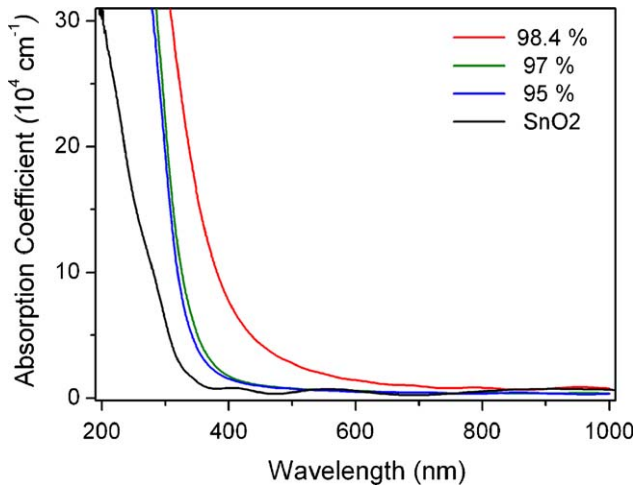

Fig. 5. Absorption spectra of SnO_2:N submicrorod arrays with different F_{N_2}.

The optical constants (n, k) are determined as follows:

$$n = \frac{1}{\sqrt{2}}\sqrt{\varepsilon_r + \sqrt{\varepsilon_r{}^2 + \varepsilon_i{}^2}}, \text{ and } k = \frac{1}{\sqrt{2}}\sqrt{-\varepsilon_r + \sqrt{\varepsilon_r{}^2 + \varepsilon_i{}^2}} \quad (6)$$

the parameters A, E_0, C, E_g, ε_∞ and P in Eqs. (4) and (5) stand for the transition matrix element, peak transition energy, broadening term, optical band gap, high frequency dielectric constant and the Cauchy principal part of the integral, respectively. The fitting results are shown in Table 4.

Fig. 6 shows the refractive index and extinction coefficient of the SnO_2:N submicrorod arrays with different nitrogen partial pressures. The refractive index of the SnO_2:N submicrorods is larger than the undoped SnO_2 film in visible wavelength range, and the increase of the refractive index after nitrogen doping can be attributed to the increase of the polarizability caused by the decreased O–Sn–O bond ionicity due to the formation of N–Sn–O bond structure [7]. From Fig. 6(a), one can see that the refractive index generally increases with the increase of N_2 flux ratio F_{N_2}. It should be note that the refractive index of the SnO_2:N with $F_{N_2} = 95\%$ shows an irregular relationship as compared with $F_{N_2} = 98.4$ and 97%. The crystal quality and microstructure, such as packing density, will affect the refractive index of the SnO_2:N submicrorods. The abnormal increase in refractive index for the SnO_2:N submicrorods grown at $F_{N_2} = 95\%$ is considered due to the enhanced crystal quality and/or packing density of the submicrorods.

From the fitting results, one can see that the band gap of SnO_2:N submicrorods decreases from 391 to 624 nm, i.e. from the UV to the visible light, when the F_{N_2} increased from 95 to 98.4%. The band

Table 4
Parameters of the TL model for fitting the optical functions of the SnO_2:N nanorod arrays.

F_{N_2}	L_1[a] (nm)	L_2 (nm)	L_3 (nm)	L_3 porosity	L_4 (nm)	L_4 porosity	A (eV)	E_0 (eV)	C (eV)	ε_∞	E_g (eV)	E_g (nm)
98.4	151.5	89.3	723.4	22.1%	25.8	60.1%	177.10	0.89	1.30	4.97	1.99	624
97	189.5	181.6	485.1	3.7%	45.4	56.3%	1112.32	1.10	1.56	3.12	2.73	455
95	70.5	52.7	700.5	27.1%	44.1	63.2%	1909.58	2.02	0.86	2.92	3.18	391

[a] L_1: the first layer thickness, similarly hereinafter.

gap of undoped SnO_2 is about 346 nm (~3.59 eV), and nitrogen doping can effectively decrease the band gap of SnO_2:N [7,9]. The SnO_2:N submicrorods have evidently higher optical absorption coefficient in visible light region as compared with the undoped SnO_2 films reported earlier [7,9], and the enhanced visible light absorption of SnO_2:N can be attributed to the band gap narrowing effect. According to the first-principle calculation, the band gap red shift can be attributed to the raising up of the top of SnO_2 valence band caused by the repulsive interaction between N 2p and O 2p states [16].

3.4. Visible light-driven photocatalysis

To demonstrate the enhanced visible light absorption of the SnO_2:N submicrorod arrays, the visible light-driven photocatalytic activity was tested following the MB decomposition as a function of irradiation time. As a comparison, the TiO_2 film was also tested.

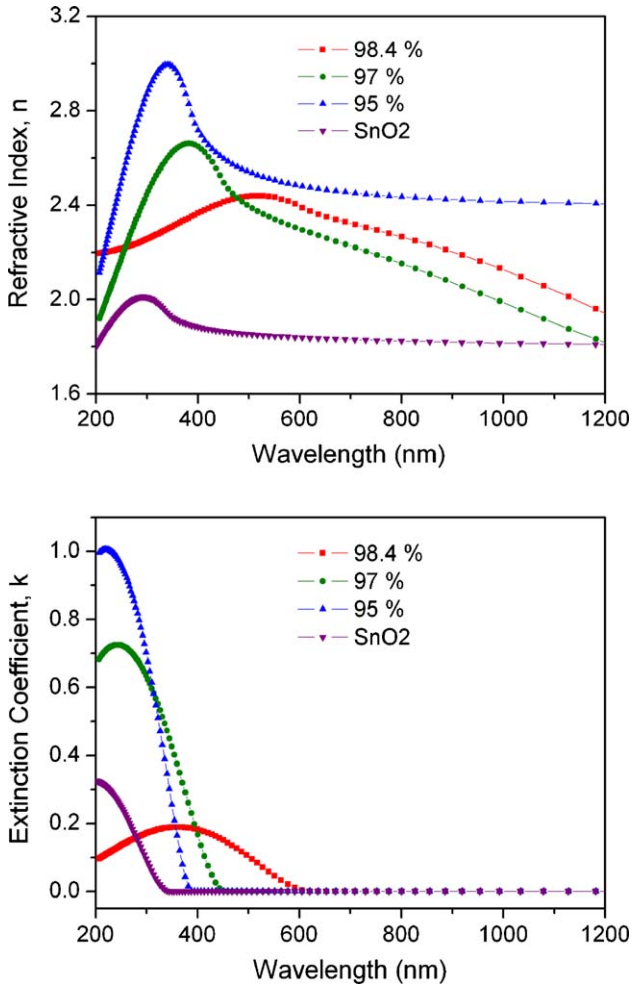

Fig. 6. Refractive index (upper), and extinction coefficient (lower) of the SnO_2:N submicrorod arrays with different F_{N_2} determined from the spectroscopy ellipsometry.

In the degradation process, the dye was photodegraded in a stepwise manner, accompanying with the color change of the solution from an initial deep blue to nearly transparent. Fig. 7(a) displays the absorption spectra of an MB solution in the presence of SnO_2:N grown with $F_{N_2} = 98.4\%$. A progressive decrease of the dye absorption with increasing irradiation time can be observed. The normalized concentration of the solution (C/C_0) is proportional to the normalized maximum absorbance (A/A_0), and therefore, we use C/C_0 instead of A/A_0 to indicate the photodegradation activity. Fig. 7(b) shows the concentration of MB as a function of irradiation time. As shown, the photodegradation of MB catalyzed by the SnO_2:N follows a first-order rate law: $-[\ln(C/C_0)] = kt$, where k is the apparent rate constant of the degradation. In the present work, k is found to be 0.56 and 0.45% min^{-1} for SnO_2:N ($F_{N_2} = 95\%$) and SnO_2:N ($F_{N_2} = 98.4\%$), respectively. Although these two curves

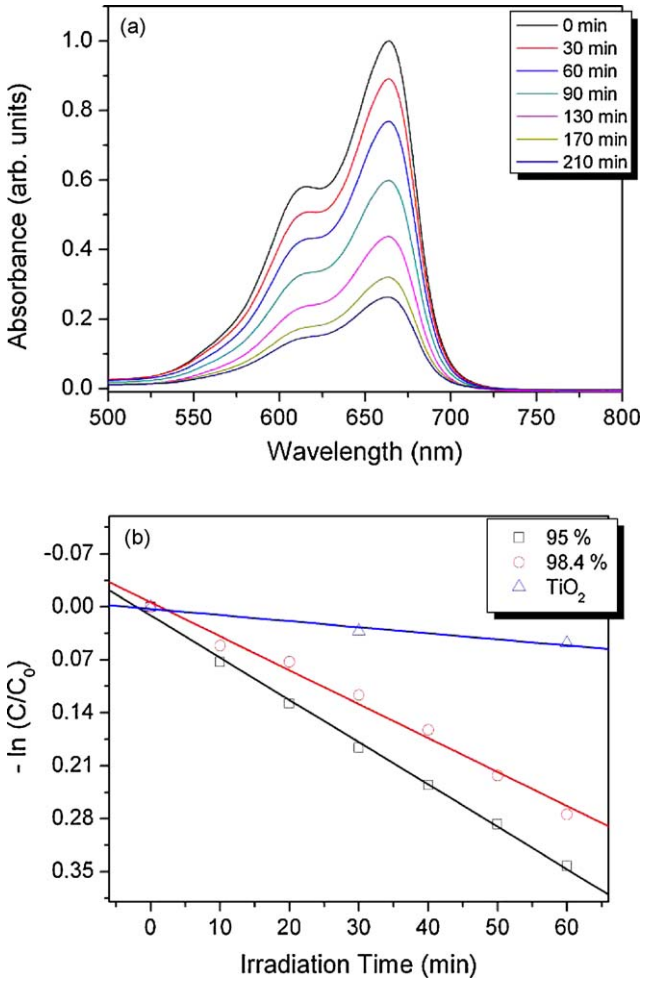

Fig. 7. (a) Absorption spectra of photocatalytically degraded methylene blue (5×10^{-5} M) as a function of irradiation time in the presence of quartz-supported SnO_2:N submicrorod with ($F_{N_2} = 98.4\%$). (b) Photodegradation kinetics of methylene blue using various SnO_2:N submicrorods synthesized in the present work.

show a progressive decay in the relative dye concentration upon irradiation, the decomposition efficiency depends on the synthesis conditions and decreases in the following order: $SnO_2 : N(F_{N_2} = 95\%) > SnO_2 : N(F_{N_2} = 98.4\%)$ ($F_{N_2} = 98.4\%$). One might expect a better photodegradation for the samples with a high dopant concentration; however, the actual surface reaction area could affect the efficiency of the photodegradation. Among the factors that affect the efficiency of the photocatalyst, the number of the excited electrons and holes created by irradiation plays an important role. The more the number of these carriers, the better the photocatalyst. The number of excited carriers is proportional to the absorption of the photocatalyst, and the photocatalytic activity should thus increase with the redshift of the absorption edge. On the other hand, the photocatalysts with high surface-to-volume (S/V) ratio can enhance the photocatalysis activity due to the large photochemical reaction area. And the surface structure tailoring and band gap engineering are two dominant methods to enhance the photocatalysis activity of semiconductor catalyst. In this study, both the band gap of SnO_2:N ($F_{N_2} = 95\%$) and SnO_2:N ($F_{N_2} = 98.4\%$) are located in visible light range, and the former have larger band gap with higher S/V ratio, while the latter have much narrower band gap with smaller S/V ratio. As can be seen from the SEM results, the SnO_2:N ($F_{N_2} = 95\%$) submicrorod surface topography, see Fig. 3(c) and (f), was characterized by a more separate granular-like texture, while a more compact morphology was observed for the SnO_2:N ($F_{N_2} = 98.4\%$), see Fig. 3(a) and (d). The surface rough layer thickness (nm) and porosity (%) determined from the spectroscopy ellipsometry are 44.1 nm, 63.2% porosity for SnO_2:N ($F_{N_2} = 95\%$) and 25.8 nm, 60.1% for SnO_2:N ($F_{N_2} = 98.4\%$), respectively. The effective surface area is typically larger for a rough surface, which means higher S/V ratio for SnO_2:N ($F_{N_2} = 95\%$). Our results demonstrate that the N-doping of SnO_2 submicrorod arrays is highly effective in visible light-driven photocatalytic activity. Miyauchi et al. investigated the MB photocatalysis degradation by SnO_2 films under intense ultraviolet (UV) illumination, and found that the SnO_2 exhibited only a small amount of oxidizing activity compared with TiO_2 [17].

The SnO_2:N single crystalline submicrorod arrays could be used as building blocks of many functional devices, especially those relevant to nanoscale energy storage and conversion materials, environmental monitor, such as dye-sensitized solar cells (DSSCs), high sensitivity chemical and biosensors, lithium ion battery, fuel cells, and nanotip field emitter. The deposition methodology of the SnO_2:N single crystalline submicrorod arrays with atomic nitrogen doping reported in this study should also be applicable to the growth of other oxide arrays, such as N-doped ZnO and N-doped TiO_2.

4. Conclusion

In summary, atomic N-doped SnO_2 submicrorod arrays have been prepared by magnetron reactive sputtering without using any catalysts. The SnO_2:N submicrorods are vertically situated on the substrate, and have nanostructured surface with a quasi-tetrahedral pyramid-like shape nanotip at the end. The growth of SnO_2:N submicrorod arrays follow a vapor–solid process, and the submicrorods are epitaxially grown on the pre-deposited SnO_2:N seed films by a layer-by-layer growth process. Nitrogen doping in SnO_2 results in both a large redshift of band gap (up to 1.9 eV). Strong photocatalytic behavior driven by visible light was demonstrated in the SnO_2:N submicrorod arrays. The SnO_2:N submicrorod arrays with visible light band gap may find potential applications in solar cells, as photocatalyst for water splitting, and as building blocks for fabrication of high sensitivity, fast response gas sensors.

Acknowledgements

This work was partially supported by the National Natural Science Foundation of China (Grant Nos. 10674137 and 50802095), the National Basic Research Program of China (Grant No. 2007CB936601) and the National Research Foundation of the Republic of Singapore (Grant No. NRF-G-CRP2007-01).

References

[1] E. Martinez-Ferrero, Y. Sakatani, C. Boissiere, D. Grosso, A. Fuertes, J. Fraxedas, C. Sanchez, Adv. Funct. Mater. 17 (2007) 3348.
[2] M. Batzill, U. Diebold, Prog. Surf. Sci. 79 (2005) 47.
[3] H.L. Xia, H.S. Zhuang, T. Zhang, D.C. Mao, Mater. Lett. 62 (2008) 1126.
[4] G. Wang, W. Lu, J.H. Li, J. Choi, Y.S. Jeong, S.Y. Choi, J.B. Park, M.K. Ryu, K. Lee, Small 2 (2006) 1436.
[5] Y. Cao, X.T. Zhang, W.S. Yang, H. Du, Y.B. Bai, T.J. Li, J.N. Yao, Chem. Mater. 12 (2000) 3445.
[6] L.X. Cao, F.J. Spiess, A.M. Huang, S.L. Suib, T.N. Obee, S.O. Hay, J.D. Freihaut, J. Phys. Chem. B 103 (1999) 2912.
[7] S.S. Pan, Y.X. Zhang, X.M. Teng, G.H. Li, L. Li, J. Appl. Phys. 103 (2008) 093103.
[8] T. Lopez-Luke, A. Wolcott, L.P. Xu, S. Chen, Z. Wen, J. Li, E. DeLaRosa, J.Z. Zhang, J. Phys. Chem. C 112 (2008) 1282.
[9] S.S. Pan, C. Ye, X.M. Teng, H.T. Fan, G.H. Li, Appl. Phys. A: Mater. Sci. Process 85 (2006) 21.
[10] PCPDFWIN, 88-0287, in: JCPDS-International Center for Diffraction Data, 2002.
[11] S.S. Pan, C. Ye, X.M. Teng, G.H. Li, J. Phys. D: Appl. Phys. 40 (2007) 4771.
[12] M. Brook, J. Kaplan, Phys. Rev. 96 (1954) 1540.
[13] Q.L. Liu, Y. Bando, J.Q. Hu, J. Cryst. Growth 306 (2007) 288.
[14] Y. Liu, M. Liu, Adv. Funct. Mater. 15 (2005) 57.
[15] Y. Inoue, M. Nomiya, O. Takai, Vacuum 51 (1998) 673.
[16] X.Q. Sun, R. Long, X.F. Cheng, X. Zhao, Y. Dai, B.B. Huang, J. Phys. Chem. C 112 (2008) 9861.
[17] M. Miyauchi, A. Nakajima, T. Watanabe, K. Hashimoto, Chem. Mater. 14 (2002) 2812.